THE JOURNAL OF PHYSICAL CHEMISTRY C
A JOURNAL OF THE AMERICAN CHEMICAL SOCIETY

pubs.acs.org/JPCC

Article

Three-Dimensional Methylhydrazinium Lead Halide Perovskites: Structural Changes and Effects on Dielectric, Linear, and Nonlinear Optical Properties Entailed by the Halide Tuning

Dawid Drozdowski, Anna Gągor, Dagmara Stefańska, Jan K. Zaręba, Katarzyna Fedoruk, Mirosław Mączka,* and Adam Sieradzki

Cite This: *J. Phys. Chem. C* 2022, 126, 1600−1610

Read Online

ACCESS | Metrics & More | Article Recommendations | Supporting Information

ABSTRACT: Three-dimensional lead halide perovskites are promising materials for optoelectronic applications. The most famous representative comprise methylammonium (MA^+) and formamidinium (FA^+) cations, but recently, this group was enlarged by methylhydrazinium (MHy^+) analogues that crystallize in polar structures at room-temperature. Properties of three-dimensional (3D) perovskites can be tuned by mixing of molecular cations or halide anions. Here, we report synthesis and physicochemical characterization of mixed-halide $MHyPbBr_xCl_{3-x}$ (x = 0.40, 0.58, 0.85, 1.33, 1.95, 2.25, and 2.55) and $MHyPbBr_{2.8}I_{0.2}$ perovskites. X-ray diffraction data show that all materials feature a polar monoclinic $P2_1$ symmetry at room temperature. With the temperature increase, all $MHyPbBr_xCl_{3-x}$ perovskites undergo a displacive phase transition to another polar orthorhombic $Pb2_1m$ phase at $T_2 \geq 318$ K. The bromine rich crystals ($x \geq 1.33$) exhibit an additional order−disorder phase transition to the archetypal cubic $Pm\bar{3}m$ phase at $T_1 \geq 409$ K. In contrast to $MHyPbBr_xCl_{3-x}$ perovskites, $MHyPbBr_{2.8}I_{0.2}$ undergoes a direct $P2_1$ to $Pm\bar{3}m$ phase transition. The temperature at which the cubic phase is stabilized, stability range of the $Pb2_1m$ phase, and distortion of the lead-halide octahedra decrease with the increase of Br^- content. The structural changes affect dielectric, conductivity, and optical properties. In particular, the Br-rich samples show switchable dielectric behavior near 410−420 K. Furthermore, the activation energy of Cl^- ionic conductivity increases with the increase of Br^- content in phases $Pb2_1m$ and $P2_1$, whereas in phase $Pm\bar{3}m$, the conductivity of Br^- ions increases with the increase of Cl^- content. The energy band gap narrows and the photoluminescence (PL) bands exhibit red shift when going from Cl to Br and then to I. Interestingly, whereas PL of the Br-rich and Cl-rich samples is dominated by bound exciton and self-trapped exciton bands, respectively, these bands are suppressed for $2.25 \geq x \geq 0.85$. The PL color is strongly tuned by doping and changes from greenish-blue for the Cl-rich samples to yellowish-green for $MHyPbBr_{2.8}I_{0.2}$. SHG studies demonstrate that doping of $MHyPbCl_3$ with Br^- ions reduces the difference between SHG signal intensities of the monoclinic and orthorhombic phases, to the extent that beyond x = 1.95, the SHG response of these phases becomes essentially the same. The relative SHG efficiencies of Br−Cl mixed materials at room temperature increase with the increase in Br content.

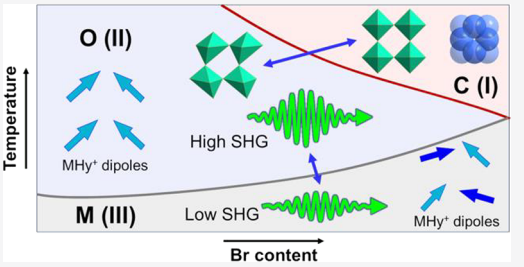

1. INTRODUCTION

Three-dimensional hybrid organic−inorganic perovskites (3D HOIPs) have been the topic of intense research efforts in recent years due to their functional properties. The general formula of 3D HOIPs is the same as for their inorganic analogues, that is, ABX_3, in which "A" cations occupy 12-fold coordinated holes between the corner-sharing BX_6 octahedra.[1−4] In HOIPs, "A" stands for an organic cation, "B" is a metal ion and "X" can be either an organic or inorganic element/group (e.g., halide, formate, azide, dicyanamide, etc.).[5−8] Among these systems, 3D lead halide HOIPs comprising methylammonium (MA^+) and formamidinium (FA^+) cations have grown to be the most explored materials. Numerous studies revealed technologically relevant physicochemical properties, such as high PL yields,[9] power conversion efficiencies of around 25%,[10,11] broad tunability of emission colors,[2] high extinction coefficients,[12] unprecedented mobility of charge carriers,[13] and the like. These properties, combined with low cost and facile synthesis, open up new perspectives for state-of-the-art applications, such as photovoltaics, light emitting devices, photodetectors, or even in photodynamic therapy.[4,14−16]

Another field of research on 3D HOIPs is the improvement of their performance via "A" site cation substitution. Such modification is an indispensable tool to allow for highly tunable modification of HOIP properties, which is usually difficult to obtain with all-inorganic counterparts. However, one should

Received: September 7, 2021
Revised: January 4, 2022
Published: January 16, 2022

https://doi.org/10.1021/acs.jpcc.1c07911
J. Phys. Chem. C 2022, 126, 1600−1610

note that there are some roadblocks to this strategy, as such modifications are limited by the steric hindrance introduced by the cubic inorganic subnetwork. A parameter that allows one to assess the stability of the 3D perovskite is the Goldschmidt tolerance factor (*TF*). Typically, *TF* should be larger than 0.8 and smaller than 1.0 in order to obtain a stable perovskite structure.[1] Thus, for 3D lead halide HOIPs, only organic cations with a relatively small effective radius, e.g., MA^+ and FA^+ (217 and 253 pm, respectively), satisfy the above rule,[3] leading to the discovery of $MAPbX_3$ and $FAPbX_3$ (X stands for Br^-, Cl^-, I^-).[17−21] Nevertheless, a seemingly finite set of small organic cations capable of affording 3D HOIPs has recently been extended by an MHy^+ cation, despite its large effective ionic radius of 264 pm. Indeed, our group has discovered 3D lead halide HOIPs comprising MHy^+ cations, i.e., $MHyPbBr_3$ and $MHyPbCl_3$. Both these perovskites feature tolerance factors higher than 1 (*TF* = 1.03 and 1.05 for Br- and Cl-analogue, respectively) and crystallize in the monoclinic, polar $P2_1$ phase at room temperature (RT).[22,23] $MHyPbBr_3$ undergoes a phase transition at 418 K to the cubic *Pm*-3*m* phase (which is archetypical of 3D perovskites) and exhibits a switchable dielectric behavior, strong second-harmonic generation (SHG) activity, thermochromism, and two-photon excited luminescence under 800 nm excitation.[22] On the other hand, $MHyPbCl_3$ undergoes a phase transition at 342 K to the $Pb2_1m$ orthorhombic space group, which is another polar and noncentrosymmetric phase. This behavior resulted in an exceptional property, i.e., enhancement of an SHG response upon transition from the low-temperature (LT) to the high-temperature (HT) phase, which has been employed to demonstrate HT switching between two SHG-active states.[23]

Recent studies on 3D HOIP analogues also revolved around alloying halogen anions at the "X" site. As a result, there is a growing body of literature demonstrating anion-tunable properties of $MAPbX_{3-x}X'_x$ and $FAPbX_{3-x}X'_x$ (X, X′ = Br^-, Cl^-, I^-) HOIPs.[24−30] For these systems, the mixing-halide approach offer tunability of the optical band gap and emission range, improved PL intensity, enhanced stability, and prolonged charge carriers' diffusion lengths while maintaining facileness of the synthesis and low fabrication cost.[25,31−34] Furthermore, mixed-halide systems can also obviate one of the crucial issues of single-halide $MA/FAPbX_3$ structures, i.e., their poor stability to adventitious water. For instance, Noh et al.[35] reported that a small Br^- content in $MAPbI_3$ thin films results in improved moisture resistance and prolonged decomposition time.

Whereas the mixing-halide approach has proven its utility for $MAPbX_{3-x}X'_x$ and $FAPbX_{3-x}X'_x$, a broader picture on various effects of halide alloying is currently lacking for $MHyPbBr_3$ and $MHyPbCl_3$ systems. Hence, we decided to synthesize mixed-halide $MHyPbBr_xCl_{3-x}$ and $MHyPbBr_xI_{3-x}$ perovskites and investigate their halide-dependent structural, dielectric, linear, and second-order nonlinear optical properties in wide temperature ranges. In particular, it is tempting to see whether this series produces similar or different halide-dependent structural characteristics from those observed for the MA^+ and FA^+-based analogues. A word of explanation is needed for $MHyPbBr_xI_{3-x}$. The 3D $MHyPbI_3$ perovskite has not been synthesized yet (our trials led to formation of yellow $MHyPbI_3$ phase with a chain structure[36]). Perhaps the only way to incorporate I^- anions into the $MHyPbX_3$ framework is to dope the $MHyPbBr_3$ phase with a small amount of I^-. Given the large ionic radius of this anion, it could affect the existence and stability of the cubic phase, which is explored here.

Herein, we report the synthesis of seven mixed-halide $MHyPbBr_xCl_{3-x}$ perovskites (x = 0.40, 0.58, 0.85, 1.33, 1.95, 2.25, and 2.55) as well as a Br−I co-doped material of formula $MHyPbBr_{2.8}I_{0.2}$. We used differential scanting calorimetry (DSC), single crystal X-ray diffraction (SCXRD), and dielectric spectroscopy to determine the uncharted phase diagram of this system and understand impact of halide alloying on the cation dynamics. Also, in this work, the impact of halide mixing on the linear absorption and PL properties was examined to establish prospects for optical band gap engineering and light-emitting applications in MHy^+-based HOIPs. Lastly, we took a closer look at effects that arise from one of the most unusual property of the MHy^+-based 3D HOIPs that is SHG response, associated with structural noncentrosymmetry.[22,23] In this way, not only the acentric identity of studied phases is confirmed but also effect of halide mixing on the relative SHG efficiency is examined.

2. EXPERIMENTAL SECTION

2.1. Materials and Instrumentation. $PbBr_2$ (98%, Sigma-Aldrich), $PbCl_2$ (98%, Sigma-Aldrich), PbI_2 (98%, Sigma-Aldrich), hydrobromic acid (48 wt % in H_2O, Sigma-Aldrich), hydrochloric acid (37 wt % in H_2O, Sigma-Aldrich), hydroiodic acid (57 wt % in H_2O, Sigma-Aldrich), methylhydrazine (98%, Sigma-Aldrich), *N*-*N*-dimethylformamide (DMF, 99.8%), and methyl acetate (99.5%, Sigma-Aldrich) were commercially available and used without further purification.

Powder XRD patterns were obtained on an X'Pert PRO X-ray diffraction system equipped with a PIXcel ultrafast line detector. The powders were measured in the reflection mode, using Cu$K\alpha$ radiation.

SCXRD experiments were carried out with Mo$K\alpha$ radiation using an Xcalibur, Atlas diffractometer. Absorption was corrected for by multi-scan methods, CrysAlis PRO 1.171.39.46 (Rigaku Oxford Diffraction, 2018). Empirical absorption correction using spherical harmonics, implemented in the SCALE3 ABSPACK scaling algorithm was applied. H atom parameters were constrained.

Heat capacity was measured using a Mettler Toledo DSC-1 calorimeter with a high resolution of 0.4 μW. Nitrogen was used as a purging gas, and the heating and cooling rates were 5 K/min. The excess heat capacity associated with the phase transitions was evaluated by subtraction from the data the baseline representing variation in the absence of the phase transitions.

Raman spectra were measured using a Bruker FT 100/S spectrometer with the YAG:Nd laser excitation (1064 nm) and were recorded with a spectral resolution of 2 cm^{-1}.

Nonlinear optical studies were performed using a laser system consisting of a Coherent Astrella Ti:Sapphire regenerative amplifier providing 800 nm pulses (75 fs pulse duration, 1 kHz repetition rate) driving a wavelength-tunable TOPAS Prime optical parametric amplifier (OPA). The output of the OPA was set to 1300 nm and was vertically polarized. A laser beam was passed through a 1200 nm longpass dielectric filter (FELH1200, Thorlabs) in order to suppress unwanted short wavelength components typically present in the OPA output.

The Kurtz−Perry test was performed at 298 K. Potassium dihydrogen phosphate (KDP) was used as an SHG reference. The single crystals of $MHyPbBr_xCl_{3-x}$, $MHyPbBr_{2.8}I_{0.2}$, and KDP were crushed with a spatula and sieved through a mini-sieve set (Aldrich), collecting a microcrystal size fraction of 125−177 μm. Next, size-graded samples were fixed in-between microscope glass slides (forming tightly packed layers), sealed,

https://doi.org/10.1021/acs.jpcc.1c07911
J. Phys. Chem. C 2022, 126, 1600−1610

and mounted to the horizontally aligned sample holder. No refractive index matching oil was used. For the Kurtz−Perry test, the average power of 1300 nm beam was equal to 343 mW (spot area of 0.5 cm^2). The employed measurement setup operates in the reflection mode. Specifically, the laser beam was directed onto the sample at 45 degrees to the sample surface and was unfocused. Emission collecting optics consisted of a Ø25.0 mm plano-convex lens of focal length 25.4 mm (Thorlabs) mounted to the 400 μm 0.22 NA glass optical fiber (Ocean Optics) and was placed along the normal to the sample surface. The distance between collection lens and the sample was equal to 30 mm. No polarizer was used; hence, the emission output of any polarization was collected. Scattered pumping radiation was suppressed with the use of a 750 nm shortpass dielectric filter (FESH0750, Thorlabs).

Temperature-resolved SHG study was performed in a separate measurement (1300 nm beam, 130−161 mW, spot area of 0.5 cm^2), in which the temperature control of the sample was performed (2−3 K step) using a Linkam LTS420 Heating/Freezing Stage. Temperature stability was equal to 0.1 K. Excitation geometry, signal collection optics, and the sample preparation protocol were the same as for the Kurtz−Perry test. The emission spectra collected in both experiments were recorded by an Ocean Optics Flame T spectrograph (200 μm slit), with a signal collection time of 2000 ms per temperature point.

Dielectric measurements were carried out using a broad band impedance Novocontrol Alpha analyzer, having a frequency range from 1 Hz up to 1 MHz. Since the obtained single crystals were not large enough to perform single-crystal dielectric measurements, pellets made of well-dried samples were measured instead. The powder was pressed into cylindrical pellets of 5 mm in diameter and from 0.5 to 0.7 mm in thickness. The surfaces of all analyzed samples were painted with silver paste to ensure good electrical contact with the electrodes. Measurements of the dielectric spectra were taken with a step of 1 K over the temperature range from 270 to 380 for the lowest Br content 280 to 440 K for higher Br contents. The temperature was controlled with a Novo-Control Quattro system using a nitrogen gas cryostat. The temperature stability of the samples was better than 0.1 K. All experiments were performed during a heating cycle at a 5 K min^{-1} rate.

The RT diffuse reflectance spectra of the powdered samples were measured using a Varian Cary 5E UV−vis−NIR spectrophotometer. Emission spectra under a 375 nm excitation line from a laser diode were measured with the Hamamatsu photonic multichannel analyzer PMA-12 equipped with a BT-CCD linear image sensor. The temperature of the samples was controlled using a Linkam THMS 600 Heating/Freezing Stage.

The elemental analysis was carried out using the scanning electron microscope FEI Nova NanoSEM 230 (FEI Company, Hillsboro, OR, USA) equipped with an EDS spectrometer (EDAX PegasusXM4) and operating acceleration voltage in the range 3.0−15 kV and spot of 2.5−3.0.

2.2. Synthesis. Single crystals of $MHyPbBr_xCl_{3-x}$ were grown using the antisolvent crystallization method. In this method, a mixture of HBr and HCl (in different ratio, adequate to the ratio of lead halides) was added dropwise to 10 mmol of methylhydrazine until pH = 7. Then, 2 mL of DMF and 10 mmol of mixed $PbBr_2$ and $PbCl_2$ powder were added under continuous stirring and this mixture was heated to 50 °C. Since not all of the lead halide precursors dissolved, 5−10 mL of DMF (depending on a sample) was added until complete dissolution of the mixture. The clear solution was placed into a glass vial, and it was placed in a second, larger vial containing methyl acetate. The lid of the outer vial was thoroughly sealed, whereas the lid of the inner vial was loosened in order to allow diffusion of methyl acetate into the precursor solution. Single crystals of $MHyPbBr_xCl_{3-x}$ were harvested after 4−5 days, filtered from a mother liquor, and dried at RT. EDS analysis revealed that the grown crystals feature bromine content $x = 0.40, 0.58, 0.85, 1.33, 1.95, 2.25$, and 2.55.

The same method was used for growing single crystals of $MHyPbBr_xI_{3-x}$. However, the precursor was prepared by adding 8.5 mmol of $PbBr_2$ and 1.5 mmol of PbI_2 to a solution containing 10 mmol of methylhydrazine dissolved in 5 mL of HBr and HI (volumetric ratio 8.5:1.5, respectively). After 5 min of continuous stirring at RT, the precursor solution became clear. Orange crystals were harvested after 5 days, filtered from a mother liquor, and dried at RT. EDS analysis revealed that the composition of these crystals is $MHyPbBr_{2.8}I_{0.2}$.

A good match of the powder X-Ray diffraction (PXRD) patterns and Raman spectra of the mixed-halide samples with the patterns and spectra recorded for $MHyPbBr_3$ and $MHyPbCl_3$ (Figures S1 and S2) proved the phase purity of the bulk samples.

3. RESULTS AND DISCUSSION

3.1. Differential Scanning Calorimetry. DSC data show the presence of two types of heat anomalies for the studied compounds (Figure 1 and Figures S3−S10). The first anomaly is observed for all $MHyPbBr_xCl_{3-x}$ samples (Figure 1a). On cooling, the temperature of this anomaly (T_2) is about ∼320 K for the Cl-rich samples (x = 0.40, 0.58, 0.85), but it strongly increases for the Br-rich samples, i.e., from 328 K for x = 1.33 to 368 K for x = 2.55 (Figure 1a). The associated changes in the enthalpy (ΔH) and entropy (ΔS) related to the phase transition at T_2 are listed in Table S1. For x ranging from 0.40 to 2.25, the values of ΔH and ΔS are about 0.65 kJ mol^{-1} and 2.0 J mol^{-1} K^{-1}, respectively. For an order−disorder phase transition, $\Delta S = R \ln(N)$, where R is the gas constant and N is the ratio of the number of configurations in the disordered and ordered phases. Using this formula, the value of N is estimated to be about 1.30. The small value of N is consistent with a displacive character of the phase transition. Since very similar values of ΔH, ΔS, and N (0.70 kJ mol^{-1}, 2.7 J mol^{-1} K^{-1}, and 1.39, respectively) were previously reported for the phase transition observed in $MHyPbCl_3$ at 329 K,[23] it is clear that doping of $MHyPbCl_3$ with Br^- up to x = 2.25 has a weak effect on the phase transition mechanism. Interestingly, this phase transition is observed even for the highest Br^- concentration (x = 2.55), although the values of N = 1.06, ΔH = 0.17 kJ mol^{-1}, and ΔS = 0.50 J mol^{-1} K^{-1} are significantly lower than for the other compositions. Thus, our data show evidence that even a low doping of Cl^- induces a displacive phase transition analogous to that observed in $MHyPbCl_3$. However, lower values of the thermal parameters suggest significantly weaker structural changes when compared to the $MHyPbBr_xCl_{3-x}$ system with x < 2.55.

The second type of heat anomaly is observed for $MHyPbBr_xCl_{3-x}$ with $x \geq 1.33$, and for $MHyPbBr_{2.8}I_{0.2}$ (Figure 1b and Figures S6−S10). In contrast to the former phase transition, the heat anomaly associated with this transition is symmetric and much more intense. Furthermore, this anomaly is observed at much higher temperatures (on cooling, T_1 ranges between 390 and 424 K, see Table S1). The average ΔH, ΔS, and N are very large, i.e., ca. 9.0 kJ mol^{-1}, 23.0 J mol^{-1} K^{-1}, and

https://doi.org/10.1021/acs.jpcc.1c07911
J. Phys. Chem. C 2022, 126, 1600−1610

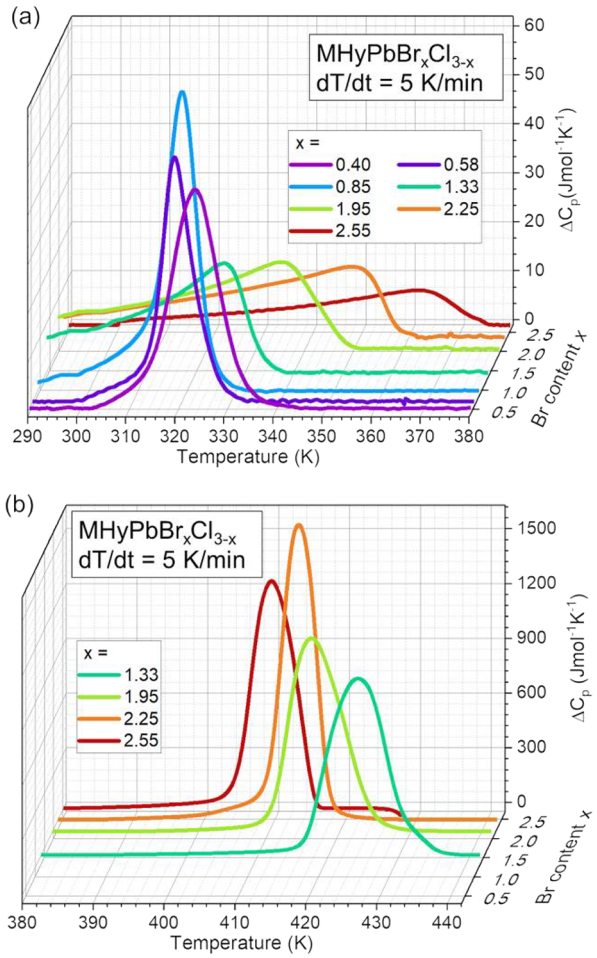

Figure 1. Change in C_p for $MHyPbBr_xCl_{3-x}$ perovskites upon cooling related to the (a) first and (b) second type of a phase transition.

17.0, respectively (Table S1), pointing to the first-order and order−disorder character of this phase transition. A similar anomaly, previously reported for $MHyPbBr_3$ at 409 K (with ΔH, ΔS, and N of 9.9 kJ mol^{-1}, 25.3 J mol^{-1} K^{-1}, and 21.0), was attributed to the $P2_1$ to $Pm\bar{3}m$ phase transition.[22] It is worth noting that doping of $MHyPbBr_3$ with Cl^- leads to the increase in T_1. Opposite behavior is observed on doping with I^- (Table S1).

3.2. Single-Crystal X-ray Diffraction. In order to establish crystal structures of the phases identified in the DSC measurements, SCXRD experiments were performed. The experimental details for $MHyPbBr_xCl_{3-x}$ (x = 0.85, 1.95, 2.55) and $MHyPbBr_{2.8}I_{0.2}$ are presented in Tables S2−S5.

$MHyPbBr_xCl_{3-x}$ systems rich in bromine ($x \geq 1.33$) adopt three polymorphic phases, while in the chloride-rich area, only two phases are observed. The HT cubic phase $Pm\bar{3}m$ (phase **I**) is centrosymmetric and isostructural with the HT phase of the $MHyPbBr_3$ analogue (Figure 2a).[22] In **I**, MHy^+ cations rotate freely, displaying no noticeable influence on the shape of PbX_6 (X = Br, Cl) octahedra. Thus, phase **I** is built of ideal PbX_6 octahedra of the O_h symmetry (Figure 2d). The polar orthorhombic $Pb2_1m$ phase (**II**) is isostructural with the HT phase of $MHyPbCl_3$.[23] In contrast to **I**, MHy^+ cations in phase **II** are oriented along one direction, giving rise to the onset of spontaneous polarization (Figure 2b). The monoclinic $P2_1$ phase (**III**), which is also polar, corresponds to the RT phases of both $MHyPbBr_3$ and $MHyPbCl_3$. If one compares crystal structures of **II** and **III**, the arrangement of polar cations in the latter is substantially reorganized. Every second MHy^+ dipole aligns more to the (010) planes than along the polar [010] direction, which diminishes polarization of this phase relative to **II** (Figure 2c). The synergistic effect of MHy^+ size and dipole orientation significantly affects crystal structures of **II** and **III**. In particular, these structures consist of $Pb(1)X_6$ and $Pb(2)X_6$ octahedra (Figure 2e,f) and the terminal N atoms of MHy^+ enter the $Pb(2)X_6$ coordination sphere, leading to higher distortion of these octahedra (Figure S11).

Experimental data from the SCXRD and DSC measurements were used together to construct the Br-Cl binary phase diagram of $MHyPbBr_xCl_{3-x}$ perovskites (Figure 3). At RT, all mixed-halide systems crystallize in phase **III**, the same as their single-halide analogues. However, neither $MHyPbBr_3$ nor $MHyPbCl_3$ showed the existence of three temperature-dependent phases.[22,23] For our mixed-halide structures, the region with all three stabilized phases starts when the content of Br^- and Cl^- is nearly equal (x = 1.33) and extends to x = 3, at which point the phase **II** vanishes. Thus, in order to stabilize phase **II** in the $MHyPbBr_3$ matrix, an incorporation of Cl^- anions appears to be crucial. On the other hand, the phase transition temperature to phase **I** increases with increasing fraction of Cl^-, and for x < 1.33, the sample decomposition occurs before the crystals reach the cubic phase. On this point, it should be emphasized that these results are opposite to those found for $MAPbBr_xCl_{3-x}$ systems, in which the increase of the Cl fraction induces a stabilization of the $Pm\bar{3}m$ phase at lower temperatures.[37]

To obtain a better grasp of temperature effects on $MAPbBr_xCl_{3-x}$ structural properties, we performed a detailed geometrical analysis of the structures. According to the Vegard's Law, for an ideal substitutional solution, the lattice parameters vary linearly with the concentration of the constituents at constant temperature (for instance, $a_{MHyPbBr1.5Cl_{1.5}} = 0.5a_{MHyPbBr_3} + 0.5a_{MHyPbCl_3}$).[38,39] In the case of our structures in phase **III**, a linear (or quasilinear) dependence of lattice parameters vs Br^- fraction is observed (Figure S12a,b). Thus, the Vegard's law is satisfied.

One should note that the difference between ionic radii of Br^- and Cl^- anions (196 and 181 pm, respectively[40]) is expected to have a non-negligible influence on the geometry of PbX_6 coordination spheres. Therefore, the octahedral angle variance (σ^2) and bond length distortion (Δ_d) values for $MHyPbBr_xCl_{3-x}$ in **III** were calculated using the Fleet's approach.[41] A comparison of $MHyPbBr_3$ and $MHyPbCl_3$ structures provides σ^2 values as follows: 14 deg^2 and 301 deg^2 for $Pb(1)Br_6$ and $Pb(2)Br_6$ octahedra, and 21 deg^2 and 314 deg^2 for $Pb(1)Cl_6$ and $Pb(2)Cl_6$.[23] In the $MHyPbBr_xCl_{3-x}$ systems, all σ^2 values for both $Pb(1)X_6$ and $Pb(2)X_6$ octahedra remain between the ones obtained for the single-halide analogues (Figure S12c). The increasing Br^- content leads to the decrease of σ^2 which means that the octahedra become less distorted. The change of Δ_d values with the increasing Br^- fraction is negligible (Δ_d for selected structures in Tables S2−S4).

The presence of the interaction between the terminal N atoms of MHy^+ with Pb calls for an investigation of the impact of this interaction on the octahedra distortion. In the single-halide analogues, the Pb(2)···N bond lengths are equal to 2.91 and 3.04 Å (2.83 and 2.89 Å) for $MHyPbBr_3$ ($MHyPbCl_3$). This is below the maximum limit for such interactions based on the survey of CCDC 2020 (Figure S13). Thus, we measured the Pb(2)···N coordination bond lengths (Figure S12d) for the

https://doi.org/10.1021/acs.jpcc.1c07911
J. Phys. Chem. C 2022, 126, 1600−1610

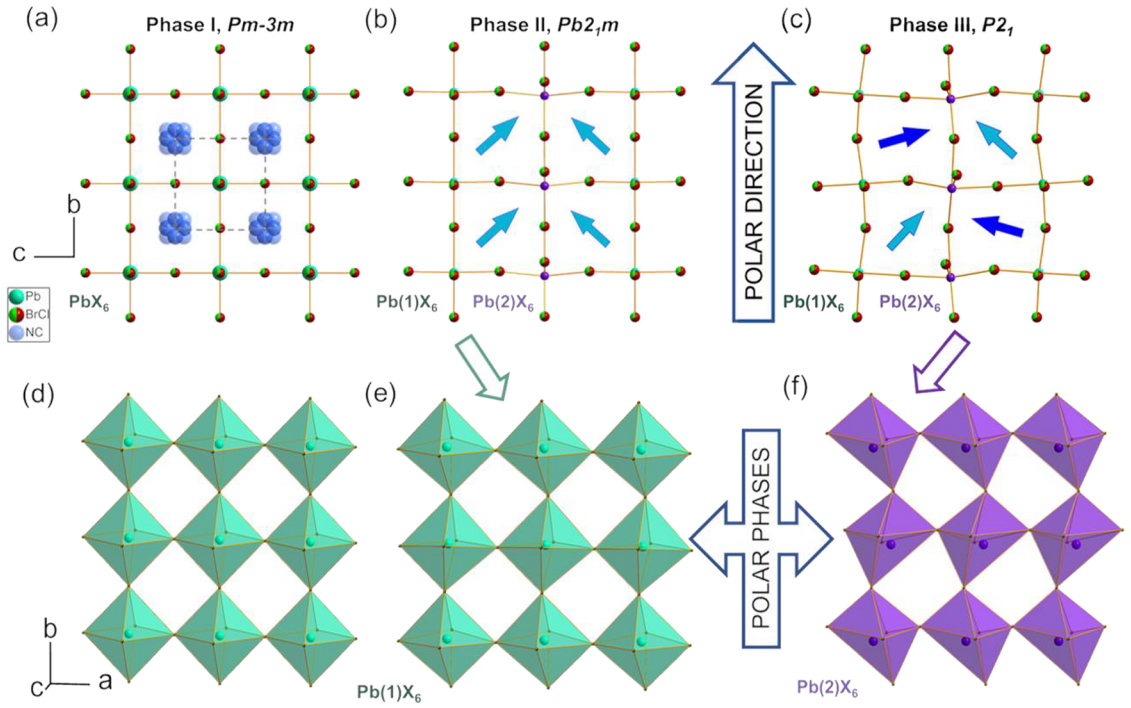

Figure 2. (a–c) Crystal structures of $MHyPbBr_xCl_{3-x}$ for phases **I**, **II**, and **III**, respectively. Arrows in (b, c) represent the location of MHy^+ dipoles. In **II** and **III**, molecules are oriented along the polar direction. (d) Single [100] layer in **I** built of PbX_6 (X = Br, Cl) octahedra. (e, f) [100] layers of (e) $Pb(1)X_6$ and (f) $Pb(2)X_6$ octahedra in both polar phases (**II**, **III**).

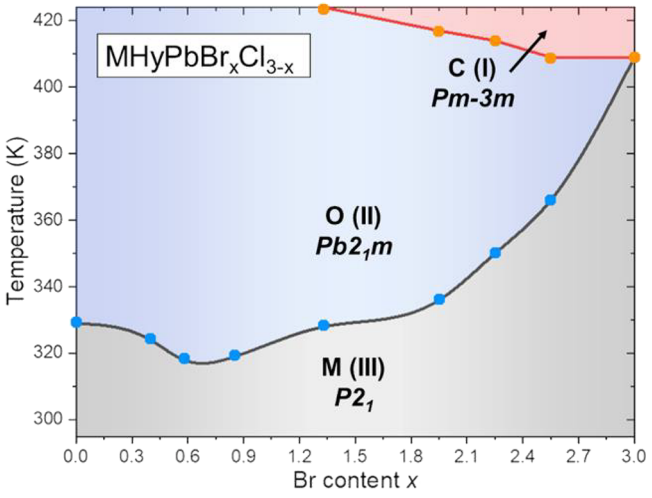

Figure 3. Phase diagram of $MHyPbBr_xCl_{3-x}$ perovskites showing cubic(C) phase **I**, orthorhombic (O) phase **II**, and monoclinic (M) phase **III**. The dots represent transition temperatures upon cooling obtained from the DSC measurements. The curves represent interpolation of the phase boundaries.

$MHyPbBr_xCl_{3-x}$ structures. Both Pb(2)···N(2) and Pb(2)···N(4) bond lengths remain between the values for boundary $MHyPbBr_3$ and $MHyPbCl_3$ structures. This observation is in line with the volume expansion of the unit cell resulting in larger voids between the octahedra. This, in turn, allows more space for the MHy^+ cations and translates to an increased Pb(2)···N distance. In order to verify this relationship, we implemented the PLATON[42] software to calculate void volumes (Figure S14). Considering the volume of the MHy^+ rotation sphere (ca. 77 Å), for our systems with $x \geq 1.95$, the void volume should be large enough to allow the free rotation of MHy^+ inside the structure. This observation agrees with our SCXRD measurements because for $x = 1.95$, we obtained stable perovskite in phase **I**, while for $x = 1.33$ the sample in **I** started to decompose (both crystals were measured at temperatures right above T_1).

SCXRD measurements of the $MHyPbBr_{2.8}I_{0.2}$ showed that at RT, it crystallizes in the monoclinic phase, space group $P2_1$, which is isostructural to **III**. According to the DSC studies, $MHyPbBr_{2.8}I_{0.2}$ undergoes a phase transition at 411 and 390 K during heating and cooling, respectively. Unfortunately, we could not obtain a model of the HT due to the poor stability of $MHyPbBr_{2.8}I_{0.2}$ above 390 K. Nevertheless, the pre-experiment made at 400 K (preceded by heating at 415 K) proved the existence of the cubic phase $Pm\bar{3}m$ (isostructural to **I**) with the lattice parameter $a = 6.046(5)$ Å. Compared to single- and mixed-halide analogues with Br^- and Cl^-, incorporation of I^- leads to stabilization of phase **I** at lower temperatures, which is in line with the largest ionic radius of I^- (220 pm[40]). The distortion parameters, σ^2 and Δ_d (Table S5), are almost identical to those of $MHyPbBr_3$.[22] Accordingly, approx. 7% fraction of I^- in the $MHyPbBr_{2.8}I_{0.2}$ systems does not affect significantly the octahedral geometry of the Pb center.

3.3. Dielectric Studies. Inspired by the phase diagram, we performed the broad band dielectric spectroscopy (BDS) studies for $MHyPbBr_xCl_{3-x}$ (x = 0.85, 1.33, 1.95, and 2.55) compounds to analyze in depth the mechanism of the observed phase transitions. The representative temperature dependences of the complex dielectric spectra of the samples with $x = 0.85$ and $x = 2.55$ are presented in Figures 4 and 5, respectively. The overall increase of both the ε' (Figures 4a and 5a) and ε'' (Figures 4b and 5b) with temperature results from increasing the contribution of the electrical conductivity and from the enhancement of this effect at higher frequencies. To suppress the effect of the electrode polarization and space charge injection phenomena, the modulus representation ($M^* = 1/\varepsilon^*$) was

https://doi.org/10.1021/acs.jpcc.1c07911
J. Phys. Chem. C 2022, 126, 1600−1610

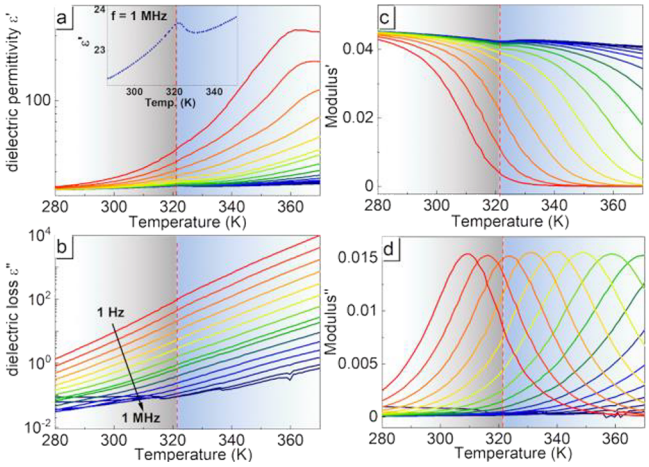

Figure 4. Temperature dependence of the (a) dielectric permittivity, (b) dielectric loss, (c) real M′, and (d) imaginary M″ components of electric modulus spectra as a function of temperature of the $MHyPbBr_{0.85}Cl_{2.15}$ pellet measured on heating. The representative curves are plotted in frequency decades between 1 Hz and 1 MHz. The changes of dielectric permittivity for 1 MHz were enlarged and are presented in the inset in (a). Colors indicate various phases.

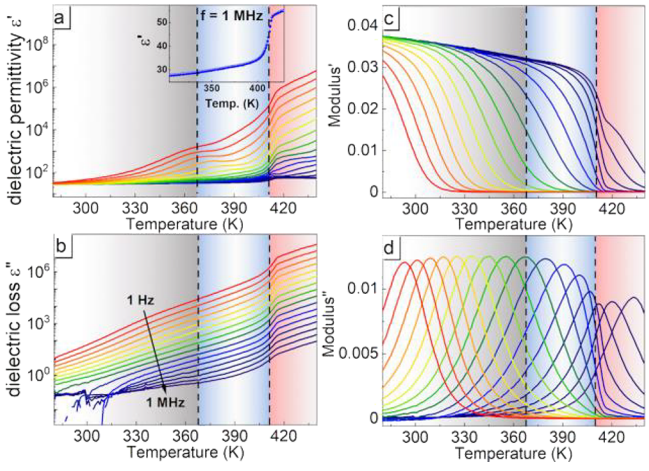

Figure 5. Temperature dependence of the (a) dielectric permittivity, (b) dielectric loss, (c) real M′, and (d) imaginary M″ components of electric modulus spectra as a function of temperature of the $MHyPbBr_{2.55}Cl_{0.45}$ pellet measured on heating. The representative curves are plotted in frequency decades between 1 Hz and 1 MHz. The changes of dielectric permittivity for 1 MHz were enlarged and are presented in the inset in (a). Colors indicate various phases.

applied (Figures 4c,d, and 5c,d).[43] A distinct anomaly of ε' and M′ at $T_2 \approx 321$ K on heating, indicating **III** to **II** phase transition for $MHyPbBr_{0.85}Cl_{2.15}$, can be observed (Figure 4a,c). The dielectric response of $MHyPbBr_{0.85}Cl_{2.15}$ is similar to that of previously published $MHyPbCl_3$.[23] By increasing the Br^- content, the dielectric response approaches the one reported for the $MHyPbBr_3$ compound.[22] Indeed, for $MHyPbBr_{1.33}Cl_{1.67}$, $MHyPbBr_{1.95}Cl_{1.05}$, and $MHyPbBr_{2.55}Cl_{0.45}$ samples, we observe only one step-like anomaly on the dielectric spectra at $T_1 \approx$ 410−430 K on heating (Figure 5a, S15a, S16a), indicating the first-order character of the **II** to **I** phase transition. The dielectric permittivity ε' and dielectric loss ε'' become strongly frequency-dependent above T_1 and increase with temperature, reaching values a few orders of magnitude higher (Figure 5a,b and Figures S15a,b and S16a,b). Furthermore, the shape of the temperature dependent complex electric modulus M* spectra revealed the emergence of an ionic and/or electronic conductivity with increasing temperature (Figure 5c,d and Figures S15c,d and S16c,d). Deeper analysis of the BDS spectra does not reveal a dipolar relaxation response coming from the movements of MHy^+ cations for $MHyPbBr_{1.33}Cl_{1.67}$ and $MHyPbBr_{1.95}Cl_{1.05}$ samples due to the high ionic and/or electronic conductivity present in these materials. Ionic halide migration has been well recognized factor affecting the electric properties in hybrid halide perovskites.[44,45]

The dielectric spectra of the $MHyPbBr_{2.55}Cl_{0.45}$ sample, measured as a function of frequency (Figure S17a−d), reveal the presence of a relaxation process, which can be well approximated by the Havriliak−Negami function (see Figure S18). A quantitative analysis of the frequency domain dielectric data allowed us to obtain the activation energies E_a of the observed processes in all studied compounds. In order to get insight into the activation energy tendency, the values for pure $MHyPbCl_3$ and $MHyPbBr_3$ were also added. It can be noticed that the measured relaxation times exhibit activation-like behavior (see Figure 6a) that can be parameterized using the Arrhenius law:

$$\tau = \tau_0 exp\left(\frac{E_a}{k_B T}\right),$$

where τ_0, E_a, and k_B denote the relaxation time at the HT limit, activation energy, and Boltzmann constant, respectively. The activation energies vs Br^- content in phases I, II, and III, are shown in Figure 6b−d, respectively. If one compares the estimated activation energies for phases II and III of $MHyPbCl_3$, it can be concluded that the symmetry changes weakly affect the energy barrier to activate the Cl^- migration. On the other hand, for $MHyPbBr_3$, the E_a in phase III is almost twice as high as that for phase I. This shows that the observed activation of the Br^- ion migration is strongly suppressed by the $P2_1$ to $Pm\bar{3}m$ symmetry change. In the mixed compounds, depending on the composition, a change in E_a is observed in each phase, which shows that halide replacement modifies the conductivity process in all phases. It can be observed that the E_a of the conductivity of Cl^- ions increases with increasing Br^- content in phases II and III. Likewise, the E_a of the conductivity of Br^- ions decreases with increasing Cl^- content in phase I (Figure 6b−d).

3.4. Linear Optical Properties. The optical absorption spectra of the investigated perovskites are composed of several bands (Figure 7a). The most red-shifted band of each sample can be attributed to the free excitonic (FE) absorption. For $MHyPbCl_3$ and $MHyPbB_3$, the excitonic absorption was observed at 373 (3.32 eV) and 469 nm (2.64 eV), respectively.[22,23] As can be seen in Figure 7a, the excitonic absorption of the $MHyPbBr_{3-x}Cl_x$ samples exhibits monotonous shift to lower energy with increasing Br^- concentration, i.e., from 389 nm (3.19 eV) for $MHyPbBr_{0.4}Cl_{2.6}$ to 457 nm (2.71 eV) for $MHyPbBr_{2.55}Cl_{0.45}$. However, the most red-shifted excitonic absorption of 484 nm (2.56 eV) is observed for $MHyPbBr_{2.8}I_{0.2}$. Thus, in spite of a small iodine concentration, the excitonic absorption exhibits a significant 15 nm shift to the red compared to pure $MHyPbBr_3$. We have also used the RT absorption spectra and Kubelka−Munk relation to estimate the energy band gaps (E_g) of the investigated perovskites (Figures 7b and 8a). In order to estimate E_g more precisely, the excitonic bands were subtracted from the spectra (Figures S19−S26). As is the case with the excitonic absorption, E_g also exhibits red shift with increasing concentration of Br^- and $MHyPbBr_{2.8}I_{0.2}$ shows

https://doi.org/10.1021/acs.jpcc.1c07911
J. Phys. Chem. C 2022, 126, 1600−1610

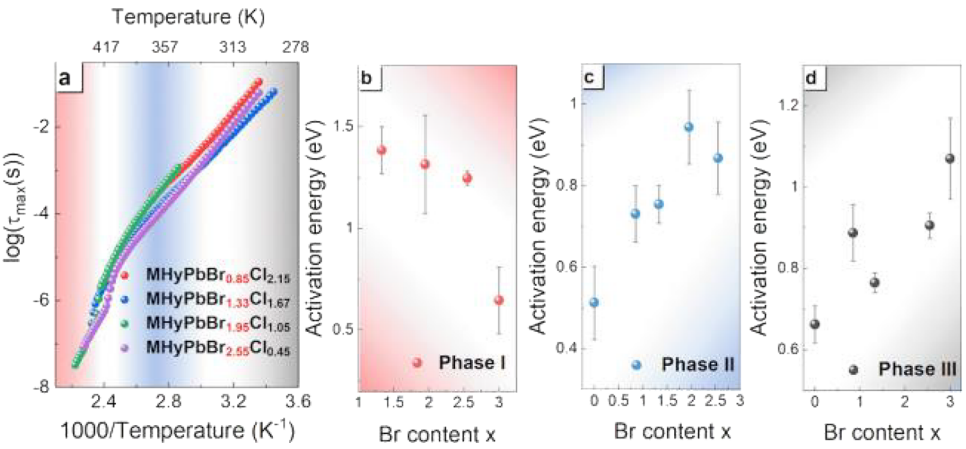

Figure 6. (a) Dependence of the maximum relaxation time as a function of inverse temperature obtained for the studied compounds. Activation energy as a function of the content of Br in (b) **I**, (c) **II**, and (d) **III**.

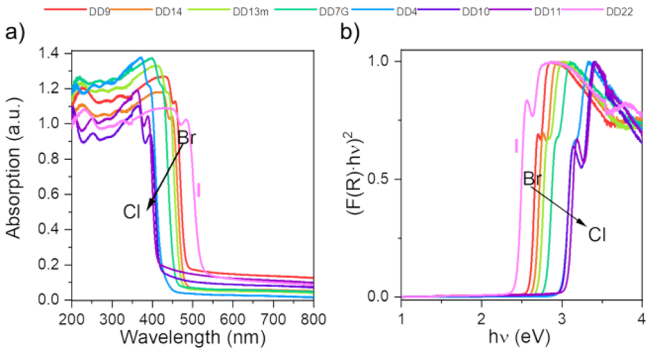

Figure 7. (a) RT diffuse absorption spectra of $MHyPbBr_xCl_{3-x}$ and $MHyPbBr_{2.8}I_{0.2}$ and (b) graphical presentation of the Kubelka−Munk function.

the narrowest band gap (Figure 8a). A similar behavior, i.e., narrowing of the band gap when going from Cl to Br and then I, was also reported for other 3D lead halides.[46]

The LT PL spectrum (Figure 8b) of $MHyPbBr_{2.8}I_{0.2}$ shows an intense and relatively broad band (FWHM = 46 nm (0.213 eV)) centered at 510 nm characteristic for BE emission.[22,47−49] In addition to this broad band, a small hump appears at 484 nm that overlaps with the excitonic absorption band and can be therefore attributed to FE recombination. The PL spectra of $MHyPbBr_xCl_{3-x}$ samples show both narrow and broad bands (Figure 8b). The narrow and the most blue-shifted band of each sample, attributed to FE recombination, moves from 399 nm for $MHyPbBr_{0.4}Cl_{2.6}$ to 453 nm for $MHyPbBr_{2.55}Cl_{0.45}$ (Figure 8c). Bands of this kind were observed at 458 and 362 nm for $MHyPbBr_3$ and $MHyPbCl_3$, respectively,[22,23] while for $MAPbBr_3$ and $FAPbBr_3$ analogues, they appeared at 545−550 nm.[50,51] In addition to the FE band, the PL spectrum of the $MHyPbBr_{2.55}Cl_{0.45}$ sample shows two additional bands at 470 and 494 nm. Their large Stokes shifts and FWHM values indicate that they can be assigned to BE states. Very similar bands were also reported for $MHyPbBr_3$, but the BE bands of $MHyPbBr_{2.55}Cl_{0.45}$ are shifted to higher energies compared to $MHyPbBr_3$ by 15.7 (85 meV) and 11.7 nm (58 meV). The BE emission disappears with increasing Cl^- content, but a new very broad PL appears around 460 nm (Figure 8b). A very large Stokes shift and FWHM value (about 0.95 eV) indicates that it cannot be assigned to a BE emission but rather to STEx states. The origin of this band is associated with the large local structure distortion and the polar nature of the mixed halides.[23]

The changes in the shape and position of the PL bands have pronounced impact on CIE coordinates. As can be seen in Figure 8d, the color of PL varies from deep blue and purplish-blue for bromine content x = 2.55−0.85 to blue and greenish blue for x = 0.58 and x = 0.40. The sample doped with iodine exhibits a yellowish-green emission with a CIE of 0.194; 0.688.

3.5. Second Harmonic Generation Studies. In this section, we move on to the investigation of the halide alloying effect on RT and temperature-resolved SHG properties (TR-SHG) of $MHyPbBr_xCl_{3-x}$ (x = 1.33, 1.95, 2.25, 2.55) and $MHyPbBr_{2.8}I_{0.2}$ materials. To this end, we employed a 1300 nm femtosecond laser radiation. While that long wavelengths of laser sources are rarely used in SHG studies of such compounds, that choice is far from accidental. In our previous report on $MHyPbBr_3$, we have observed that the use of shorter laser wavelengths, such as 800 nm, efficiently excites luminescence through the two-photon absorption (2PA) mechanism.[22] As a result, strong up-converted luminescence obscured much weaker in intensity SHG signal. Also, the produced SHG (400 nm) falls directly in the optical band gap and so is effectively attenuated by one-photon absorption resonances. Both these effects are significantly suppressed at 1300 nm, for two reasons. Excitation at 1300 nm corresponds to regions of three-photon and multi-photon absorption, and these processes are weaker than 2PA. Additionally, the produced SHG sits at 650 nm, and as can be seen in the reflectance spectra discussed in the previous section (Figure 7), this spectral region is free of one-photon absorption bands. It follows that the produced SHG is not subject to self-absorption.

RT Kurtz−Perry powder tests[52] on size-graded microcrystalline samples have been performed to reveal the effect of halide mixing of the relative efficiency of generation of second harmonic of radiation (Figure 9a). Experimental spectra are presented in Figure S27. It turns out that relative SHG efficiency (expressed vs that of KDP) for halide-alloyed samples remains within the range imposed by pure-halide phases $MHyPbCl_3$ ($0.03 \cdot I(2\omega)_{KDP}$) and $MHyPbBr_3$ ($0.18 \cdot I(2\omega)_{KDP}$). One sees that bromine doping into the $MHyPbCl_3$ matrix starts to impact I_{SHG} values only at x = 1.95 ($0.02 \cdot I(2\omega)_{KDP}$) and the phase with x = 2.55 features the same relative SHG efficiency ($0.21 \cdot I(2\omega)_{KDP}$) as $MHyPbBr_3$, within experimental error. In the case of $MHyPbBr_{2.8}I_{0.2}$, the obtained I_{SHG} value ($0.015 \cdot I(2\omega)_{KDP}$) is

https://doi.org/10.1021/acs.jpcc.1c07911
J. Phys. Chem. C 2022, 126, 1600−1610

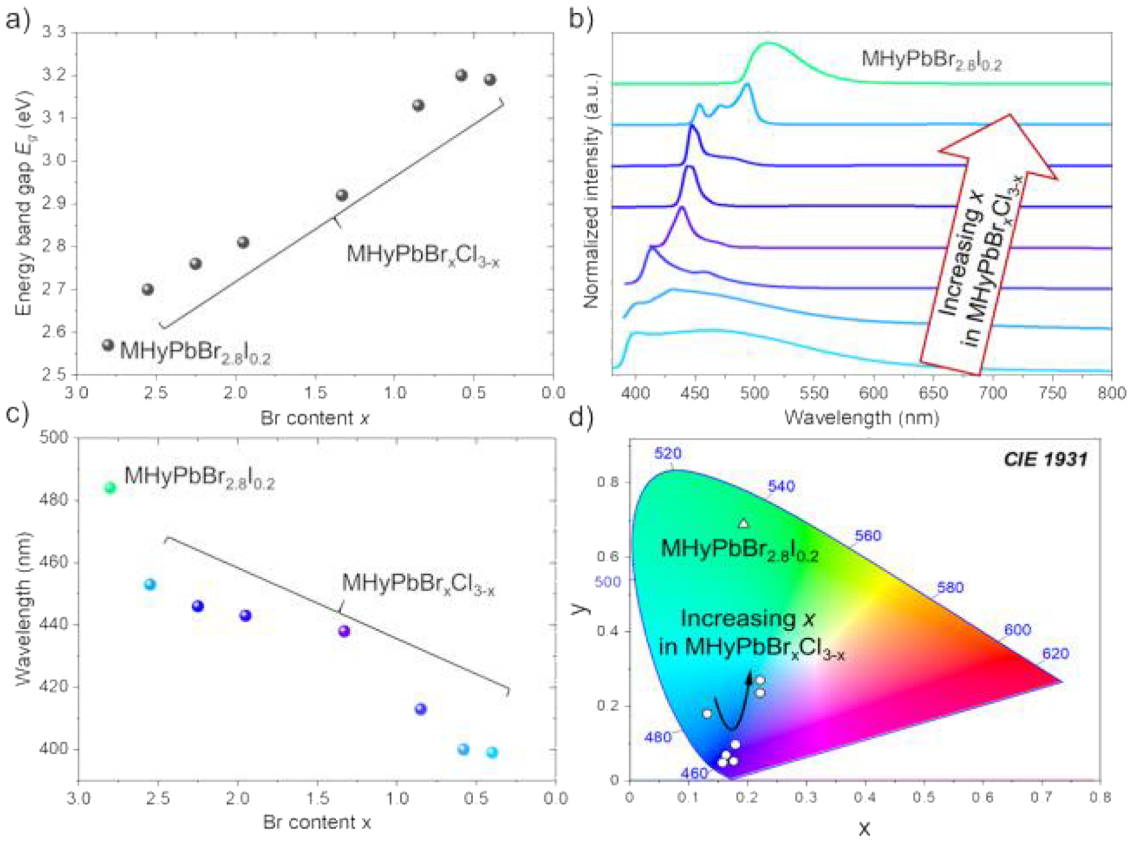

Figure 8. (a) Values of the energy band gap E_g of the investigated compounds. (b) PL spectra of MHyPbBr$_x$Cl$_{3-x}$ and MHyPbBr$_{2.8}$I$_{0.2}$ recorded at 80 K, (c) changes of FE band position with sample composition, and (d) CIE coordinates of the investigated samples.

still close to that of MHyPbBr$_3$, and likely low doping of iodine has little effect on SHG efficiency.

It was tempting to see how the temperature-dependent SHG response evolves in Br−Cl co-doped samples. To this end, TR-SHG measurements have been performed for MHyPbBr$_x$Cl$_{3-x}$ samples with x = 1.33, 1.95, 2.25, 2.55 (Figure 9b,c and Figures S28−S37). We will discuss in detail results for MHyPbBr$_{1.33}$Cl$_{1.67}$ and MHyPbBr$_{1.95}$Cl$_{1.05}$ only (Figure 9b,c), since the latter compositions feature essentially similar TR-SHG plots (Figures S32 and S35, respectively), which is in agreement with the derived phase diagram (vide supra, Figure 3).

In the case of MHyPbBr$_{1.33}$Cl$_{1.67}$, one sees that the SHG response rises upon transition from the monoclinic phase **III** to orthorhombic phase **II**. If one compares data points close to the phase transition temperature (ca. 330 K), the SHG enhancement is merely of 5%. The same behavior was previously identified for MHyPbCl$_3$, but for this compound, the SHG signal increased by about 40%; that high difference in signal strengths was sufficient to demonstrate temperature switching between two SHG states.[23] This result gave us a hint that doping of MHyPbCl$_3$ with Br$^-$ decreases the SHG contrast between monoclinic and orthorhombic crystal phases, so we examined materials with higher bromine content to verify this hypothesis.

The TR-SHG plot recorded for MHyPbBr$_{1.95}$Cl$_{1.05}$ shows very weakly marked inflection near 330 K in the heating run, indicative of a phase transition from **III** to **II**. Note that for higher Br$^-$ contents (x = 2.25, 2.55, see Figures S32 and S35, respectively), **III** to **II** phase transition is not visible in TR- SHG plots at all (though detectable by DSC, BDS and X-ray crystallography), as the change in SHG response due to phase transition is so small that is obscured by the signal's ripple.

This set of results tells us that stepwise enrichment of the MHyPbCl$_3$ matrix with Br$^-$ suppresses SHG contrast between monoclinic and orthorhombic crystal phases. Application-wise, this effect cannot be seen as useful if a high difference between the SHG signals is required, e.g., in devices employing switching of quadratic NLO response.

Structural studies shown that MHyPbBr$_{1.95}$Cl$_{1.05}$, MHyPbBr$_{2.25}$Cl$_{0.75}$, and MHyPbBr$_{2.55}$Cl$_{0.45}$ feature not only noncentrosymmetric orthorhombic (**II**) and monoclinic (**III**) phases but also a centrosymmetric cubic phase (**I**). Indeed, this is reflected in TR-SHG results (see Figure 9c and Figures S32 and S35, respectively). As seen in these Figures, transition from **II** to **I** results in the complete suppression of the SHG response. An analogous behavior is noted in TR-SHG results for MHyPbBr$_{2.8}$I$_{0.2}$ (Figures S38-S40), which confirms that the cubic phase of this HOIP halide alloy is also centrosymmetric.

Quite a striking observation, which can be made for x = 1.95, 2.25, 2.55, and MHyPbBr$_{2.8}$I$_{0.2}$ compositions, is the significant enhancement (3−5-fold) of the SHG response seen in their cooling runs (**I** to **II** transition) relative to heating runs. Note that this is observed only for materials that feature cubic phase **I** and only when samples are heated to cross their respective T_1 temperatures to reach this phase. While at present, we do not know specific origins of this phenomenon, we speculate that transition between these phases generates defects that act as SHG active centers upon restoration of phase **II**.

4. CONCLUSIONS

In this contribution, we took a closer look at effects of halide alloying in HOIPs comprising MHy$^+$ cations: Br−Cl systems of formula MHyPbBr$_x$Cl$_{3-x}$ (x = 0.40, 0.58, 0.85, 1.33, 1.95, 2.25,

https://doi.org/10.1021/acs.jpcc.1c07911
J. Phys. Chem. C 2022, 126, 1600−1610

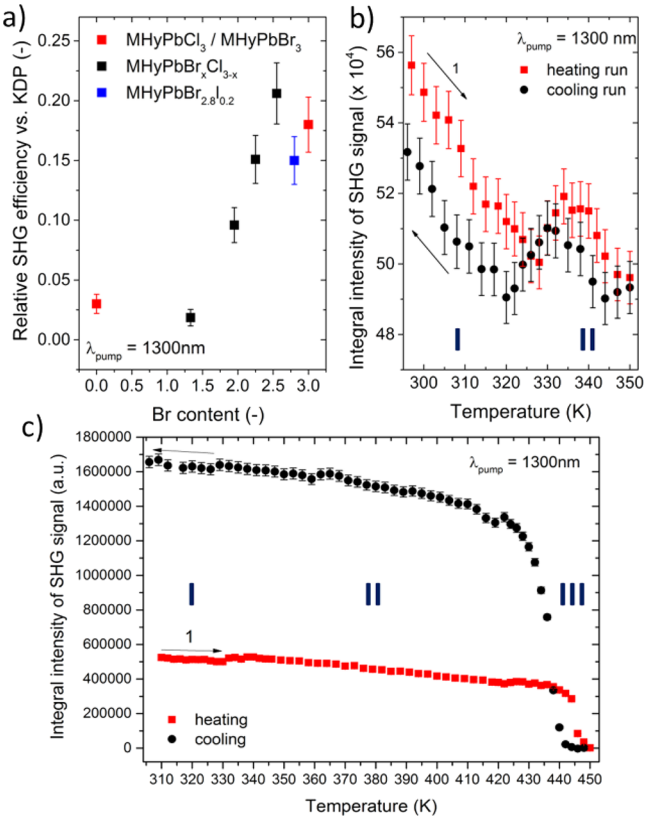

Figure 9. (a) Plot of relative SHG efficiencies expressed vs KDP for $MHyPbBr_xCl_{3-x}$ (x = 0, 1.33, 1.95, 2.25, 2.55, 3) and $MHyPbBr_{2.8}I_{0.2}$. Note that relative SHG efficiencies for $MHyPbBr_3$ and $MHyPbCl_3$ are taken from previous reports.[22,23] (b) Plots of integral intensities of the SHG signal of $MHyPbBr_{1.33}Cl_{1.67}$ for the heating run (296−350 K, red squares) and cooling run (350−294 K, black squares). (c) Plots of integral intensities of the SHG signal of $MHyPbBr_{1.95}Cl_{1.05}$ for the heating run (306−450 K, red squares) and cooling run (450−306 K, black squares).

and 2.55) and a single representative of Br−I compounds, i.e., $MHyPbBr_{2.8}I_{0.2}$.

SCXRD data showed that lattice parameters vary linearly with the x value at constant temperature, and thus $MHyPbBr_xCl_{3-x}$ systems fulfill Vegard's Law and can be thought of as ideal substitutional solid-state solutions. X-ray diffraction supported by SHG results evidence that all $MHyPbBr_xCl_{3-x}$ and $MHyPbBr_{2.8}I_{0.2}$ perovskites crystallize at RT in a polar $P2_1$ structure (**III**). For the Br-rich compositions ($x \geq 1.33$) both HT phases of $MHyPbBr_3$ and $MHyPbCl_3$ are observed (cubic $Pm\bar{3}m$ (**I**) for $T_1 \geq 409$ K and orthorhombic $Pb2_1m$ (**II**) for $T_2 \geq 318$ K, respectively), while for lower Br content ($x < 1.33$), phase **I** vanishes. This behavior is opposite to that displayed by $MAPbBr_xCl_{3-x}$ systems, for which the increase of Cl^- content induced a stabilization of the cubic phase at lower temperatures. The above observations, as well as the analysis of geometrical parameters, led to a conclusion that the presence of the cubic phase strongly depends on the volume of the voids in-between the PbX_6 octahedra, in which MHy^+ cations are placed. Phase **II**, which was not observed for $MHyPbBr_3$, starts to appear at small doping of Cl^- ions. In a similar manner to $MHyPbBr_3$, $MHyPbBr_{2.8}I_{0.2}$ undergoes a direct phase transition from **III** to **I** but at lower temperature T_1 = 390 K.

Dielectric studies confirm the (x,T) phase diagram and provide evidence for the significant contribution of ionic/electronic conductivity into dielectric response of mixed-halide MHy^+-based HOIPs. In phases **II** and **III**, the activation energy of Cl^- conductivity increases along with the Br^- doping, whereas in phase **I**, the activation energy of Br^- conductivity decreases with increasing Cl^- content.

Linear optical studies display systematic narrowing of the optical band gap and red shift of excitonic absorption with increasing Br^- concentration and then on iodine doping, i.e., the excitonic absorption changes from 3.19 eV for $MHyPbBr_{0.4}Cl_{2.6}$ to 2.56 eV for $MHyPbBr_{2.8}I_{0.2}$. PL properties also depend strongly on the chemical composition. First, the PL spectra of $MHyPbBr_{2.8}I_{0.2}$ and $MHyPbBr_{2.55}Cl_{0.45}$ samples are dominated by broad bands characteristic for BE emission. The BE emission disappears with increasing Cl^- content, and the spectra are dominated by narrow FE emission for $2.25 \geq x \geq 0.85$. On further increase of Cl^- content, a new very broad PL appears around 460 nm that can be attributed to STEx states. Second, PL bands exhibit red shift with increasing Br^- or I^- content. These changes lead to strong tunability of the PL color, from greenish-blue for the Cl-rich samples to yellowish-green for $MHyPbBr_{2.8}I_{0.2}$.

TR-SHG studies revealed that doping of $MHyPbCl_3$ with Br^- gradually decreases the difference between SHG intensities provided by monoclinic and orthorhombic crystal phases, to the point that no measurable difference in SHG intensities between these crystal phases is observed. Comparison of SHG efficiencies measured at RT for $MHyPbBr_xCl_{3-x}$ halide alloys shows that there is no additional gain in SHG efficiency for these hybrids. Indeed, relative SHG efficiencies of halide-alloyed HOIPs remain within the range determined for $MHyPbCl_3$ and $MHyPbBr_3$ and are higher for the Br-rich samples.

Bearing in mind the wide-ranging investigation of 3D HOIPs in terms of numerous technological applications in materials science, our work has clearly revealed the usefulness of the halide alloying approach. We demonstrated large tunability of structural, optical, and dielectric properties of the newcomers in the perovskite family, i.e., lead halide HOIPs comprising MHy^+ cations.

■ ASSOCIATED CONTENT

Supporting Information

The Supporting Information is available free of charge at https://pubs.acs.org/doi/10.1021/acs.jpcc.1c07911.

(Tables S1−S6) Parameters obtained from DSC, SCXRD experimental details, and energy band gap values; (Figures S1−S40) PXRD patterns, Raman spectra, DSC traces, geometric parameters, frequency dependences of the complex dielectric permittivity and electrical modulus, Kubelka−Munk functions, experimental SHG spectra, and TR-SHG plots (PDF)

CIF files of $MHyPbBr_xCl_{3-x}$ in **I**, **II**, and **III**, and $MHyPbBr_{2.8}Cl_{0.2}$. CCDC 2065131−2065141, 2073876 (ZIP)

■ AUTHOR INFORMATION

Corresponding Author

Mirosław Mączka − *Institute of Low Temperature and Structure Research, Polish Academy of Sciences, 50-422 Wrocław, Poland;* orcid.org/0000-0003-2978-1093; Phone: +48 71 3954 161; Email: m.maczka@intibs.pl; Fax: +48 71 3441 029

https://doi.org/10.1021/acs.jpcc.1c07911
J. Phys. Chem. C 2022, 126, 1600−1610

Authors

Dawid Drozdowski − *Institute of Low Temperature and Structure Research, Polish Academy of Sciences, 50-422 Wrocław, Poland;* orcid.org/0000-0001-5918-5503

Anna Gągor − *Institute of Low Temperature and Structure Research, Polish Academy of Sciences, 50-422 Wrocław, Poland*

Dagmara Stefańska − *Institute of Low Temperature and Structure Research, Polish Academy of Sciences, 50-422 Wrocław, Poland;* orcid.org/0000-0002-1051-3761

Jan K. Zaręba − *Advanced Materials Engineering and Modeling Group, Wroclaw University of Science and Technology, 50-370 Wrocław, Poland;* orcid.org/0000-0001-6117-6876

Katarzyna Fedoruk − *Department of Experimental Physics, Wrocław University of Science and Technology, 50-370 Wrocław, Poland*

Adam Sieradzki − *Department of Experimental Physics, Wrocław University of Science and Technology, 50-370 Wrocław, Poland;* orcid.org/0000-0003-4136-5754

Complete contact information is available at: https://pubs.acs.org/10.1021/acs.jpcc.1c07911

Author Contributions

The manuscript was written through contributions of all authors. All authors have given approval to the final version of the manuscript.

Notes

The authors declare no competing financial interest.

■ ACKNOWLEDGMENTS

This research was supported by the National Science Center (Narodowe Centrum Nauki) in Poland under project no. 2019/35/B/ST5/00043. J.K.Z. acknowledges financial support from Wroclaw University of Science and Technology.

■ REFERENCES

(1) Mitzi, D. B. Synthesis, Structure, and Properties of Organic-Inorganic Perovskites and Related Materials. In *Progress in Inorganic Chemistry*; Karlin, K. D..; Wiley, 1999; Vol. *48*, pp. 1−121.

(2) Li, W.; Wang, Z.; Deschler, F.; Gao, S.; Friend, R. H.; Cheetham, A. K. Chemically Diverse and Multifunctional Hybrid Organic-Inorganic Perovskites. *Nat. Rev. Mater.* **2017**, *2*, 16099.

(3) Saparov, B.; Mitzi, D. B. Organic-Inorganic Perovskites: Structural Versatility for Functional Materials Design. *Chem. Rev.* **2016**, *116*, 4558−4596.

(4) Zhao, X.; Ng, J. D. A.; Friend, R. H.; Tan, Z. K. Opportunities and Challenges in Perovskite Light-Emitting Devices. *ACS Photonics* **2018**, *5*, 3866−3875.

(5) Poglitsch, A.; Weber, D. Dynamic Disorder in Methylammonium-trihalogenoplumbates (II) Observed by Millimeter-Wave Spectroscopy. *J. Chem. Phys.* **1987**, *87*, 6373−6378.

(6) Sletten, E.; Jensen, L. H. The Crystal Structure of Dimethylammonium Copper(II) Formate, $NH_2(CH_2)_2[Cu(OOCH)_3]$. *Acta Crystallogr., B* **1973**, *29*, 1752−1756.

(7) Tong, M. L.; Ru, J.; Wu, Y. M.; Chen, X. M.; Chang, H. C.; Mochizuki, K.; Kitagawa, S. Cation-Templated Construction of Three-Dimensional α-Po Cubic-Type $[M(dca)_3]$- Networks. Syntheses, Structures and Magnetic Properties of $A[M(dca)_3]$ (dca = Dicyanamide; for A = Benzyltributylammonium, M = Mn^{2+}, Co^{2+}; for A = Benzyltriethylammonium, M = Mn^{2+}). *New J. Chem.* **2003**, *27*, 779−782.

(8) Zhao, X. H.; Huang, X. C.; Zhang, S. L.; Shao, D.; Wei, H. Y.; Wang, X. Y. Cation-Dependent Magnetic Ordering and Room-Temperature Bistability in Azido-Bridged Perovskite-Type Compounds. *J. Am. Chem. Soc.* **2013**, *135*, 16006−16009.

(9) Wang, W.; Zhang, Y.; Wu, W.; Liu, X.; Ma, X.; Qian, G.; Fan, J. Quantitative Modeling of Self-Assembly Growth of Luminescent Colloidal $CH_3NH_3PbBr_3$ Nanocrystals. *J. Phys. Chem. C* **2019**, *123*, 13110−13121.

(10) Lin, R.; Xiao, K.; Qin, Z.; Han, Q.; Zhang, C.; Wei, M.; Saidaminov, M. I.; Gao, Y.; Xu, J.; Xiao, M.; et al. Monolithic All-Perovskite Tandem Solar Cells with 24. 8% Efficiency Exploiting Comproportionation to Suppress Sn(II) Oxidation in Precursor Ink. *Nat. Energy* **2019**, *4*, 864−873.

(11) NREL *Best Research-Cell Efficiency Chart* https://www.nrel.gov/pv/assets/pdfs/best-research-cell-efficiencies.20190802.pdf (accessed Mar 14, 2021).

(12) Ball, J. M.; Lee, M. M.; Hey, A.; Snaith, H. J. Low-Temperature Processed Meso-Superstructured to Thin-Film Perovskite Solar Cells. *Energy Environ. Sci.* **2013**, *6*, 1739−1743.

(13) Stranks, S. D.; Eperon, G. E.; Grancini, G.; Menelaou, C.; Alcocer, M. J. P.; Leijtens, T.; Herz, L. M.; Petrozza, A.; Snaith, H. J. Electron-Hole Diffusion Lengths Exceeding 1 Micrometer in an Organometal Trihalide Perovskite Absorber. *Science* **2013**, *342*, 341−344.

(14) Mehdi, H.; Mhamdi, A.; Hannachi, R.; Bouazizi, A. $MAPbBr_3$ Perovskite Solar Cells: Via a Two-Step Deposition Process. *RSC Adv.* **2019**, *9*, 12906−12912.

(15) Cao, M.; Tian, J.; Cai, Z.; Peng, L.; Yang, L.; Wei, D. Perovskite Heterojunction Based on $CH_3NH_3PbBr_3$ Single Crystal for High-Sensitive Self-Powered Photodetector. *Appl. Phys. Lett.* **2016**, *109*, 233303.

(16) Wang, F.; Cao, Y.; Chen, C.; Chen, Q.; Wu, X.; Li, X.; Qin, T.; Huang, W. Materials Toward the Upscaling of Perovskite Solar Cells: Progress, Challenges, and Strategies. *Adv. Funct. Mater.* **2018**, *28*, 1803753.

(17) Zhumekenov, A. A.; Saidaminov, M. I.; Haque, M. A.; Alarousu, E.; Sarmah, S. P.; Murali, B.; Dursun, I.; Miao, X. H.; Abdelhady, A. L.; Wu, T.; et al. Formamidinium Lead Halide Perovskite Crystals with Unprecedented Long Carrier Dynamics and Diffusion Length. *ACS Energy Lett.* **2016**, *1*, 32−37.

(18) Eperon, G. E.; Stranks, S. D.; Menelaou, C.; Johnston, M. B.; Herz, L. M.; Snaith, H. J. Formamidinium Lead Trihalide: A Broadly Tunable Perovskite for Efficient Planar Heterojunction Solar Cells. *Energy Environ. Sci.* **2014**, *7*, 982−988.

(19) Liu, M.; Johnston, M. B.; Snaith, H. J. Efficient Planar Heterojunction Perovskite Solar Cells by Vapour Deposition. *Nature* **2013**, *501*, 395−398.

(20) Wu, X.; Trinh, M. T.; Niesner, D.; Zhu, H.; Norman, Z.; Owen, J. S.; Yaffe, O.; Kudisch, B. J.; Zhu, X. Y. Trap States in Lead Iodide Perovskites. *J. Am. Chem. Soc.* **2015**, *137*, 2089−2096.

(21) Hanusch, F. C.; Wiesenmayer, E.; Mankel, E.; Binek, A.; Angloher, P.; Fraunhofer, C.; Giesbrecht, N.; Feckl, J. M.; Jaegermann, W.; Johrendt, D.; et al. Efficient Planar Heterojunction Perovskite Solar Cells Based on Formamidinium Lead Bromide. *J. Phys. Chem. Lett.* **2014**, *5*, 2791−2795.

(22) Mączka, M.; Ptak, M.; Gągor, A.; Stefańska, D.; Zaręba, J. K.; Sieradzki, A. Methylhydrazinium Lead Bromide: Noncentrosymmetric Three-Dimensional Perovskite with Exceptionally Large Framework Distortion and Green Photoluminescence. *Chem. Mater.* **2020**, *32*, 1667−1673.

(23) Mączka, M.; Gagor, A.; Zaręba, J. K.; Stefanska, D.; Drozd, M.; Balciunas, S.; Šimėnas, M.; Banys, J.; Sieradzki, A. Three-Dimensional Perovskite Methylhydrazinium Lead Chloride with Two Polar Phases and Unusual Second-Harmonic Generation Bistability above Room Temperature. *Chem. Mater.* **2020**, *32*, 4072−4082.

(24) Rosales, B. A.; Men, L.; Cady, S. D.; Hanrahan, M. P.; Rossini, A. J.; Vela, J. Persistent Dopants and Phase Segregation in Organolead Mixed-Halide Perovskites. *Chem. Mater.* **2016**, *28*, 6848−6859.

(25) Zhang, M.; Yu, H.; Lyu, M.; Wang, Q.; Yun, J. H.; Wang, L. Composition-Dependent Photoluminescence Intensity and Prolonged Recombination Lifetime of Perovskite $CH_3NH_3PbBr_{3-x}Cl_x$ Films. *Chem. Commun.* **2014**, *50*, 11727−11730.

(26) Madjet, M. E. A.; Akimov, A. V.; El-Mellouhi, F.; Berdiyorov, G. R.; Ashhab, S.; Tabet, N.; Kais, S. Enhancing the Carrier Thermalization Time in Organometallic Perovskites by Halide Mixing. *Phys. Chem. Chem. Phys.* **2016**, *18*, 5219−5231.
(27) Gil-Escrig, L.; Miquel-Sempere, A.; Sessolo, M.; Bolink, H. J. Mixed Iodide-Bromide Methylammonium Lead Perovskite-Based Diodes for Light Emission and Photovoltaics. *J. Phys. Chem. Lett.* **2015**, *6*, 3743−3748.
(28) Fedeli, P.; Gazza, F.; Calestani, D.; Ferro, P.; Besagni, T.; Zappettini, A.; Calestani, G.; Marchi, E.; Ceroni, P.; Mosca, R. Influence of the Synthetic Procedures on the Structural and Optical Properties of Mixed-Halide (Br, I) Perovskite Films. *J. Phys. Chem. C* **2015**, *119*, 21304−21313.
(29) Karlsson, M.; Yi, Z.; Reichert, S.; Luo, X.; Lin, W.; Zhang, Z.; Bao, C.; Zhang, R.; Bai, S.; Zheng, G.; et al. Mixed Halide Perovskites for Spectrally Stable and High-Efficiency Blue Light-Emitting Diodes. *Nat. Commun.* **2021**, *12*, 361.
(30) Ebadi, M.; Sefidi, P. Y.; Samadifar, A.; Salari, D.; Darbandi, M.; Hosseini, M. G. Influence of Lead (II) Chloride and/or Lead (II) Bromide Entrance on the Efficiency and Stability of Methyl Ammonium Lead Triiodide Perovskite Solar Cell: Comparative Study of the Halide Composition and Substitution Percentage. *Opt. Mater.* **2021**, *113*, 110888.
(31) Edri, E.; Kirmayer, S.; Kulbak, M.; Hodes, G.; Cahen, D. Chloride Inclusion and Hole Transport Material Doping to Improve Methyl Ammonium Lead Bromide Perovskite-Based High Open-Circuit Voltage Solar Cells. *J. Phys. Chem. Lett.* **2014**, *5*, 429−433.
(32) Hu, Z.; An, Q.; Xiang, H.; Aigouy, L.; Sun, B.; Vaynzof, Y.; Chen, Z. Enhancing the Efficiency and Stability of Triple-Cation Perovskite Solar Cells by Eliminating Excess $PbI_2$from the Perovskite/Hole Transport Layer Interface. *ACS Appl. Mater. Interfaces* **2020**, *12*, 54824−54832.
(33) Yuan, J.; Hazarika, A.; Zhao, Q.; Ling, X.; Moot, T.; Ma, W.; Luther, J. M. Metal Halide Perovskites in Quantum Dot Solar Cells: Progress and Prospects. *Joule* **2020**, *4*, 1160−1185.
(34) Brivio, F.; Caetano, C.; Walsh, A. Thermodynamic Origin of Photoinstability in the $CH_3NH_3Pb(I_{1-X}Br_x)_3$ Hybrid Halide Perovskite Alloy. *J. Phys. Chem. Lett.* **2016**, *7*, 1083−1087.
(35) Noh, J. H.; Im, S. H.; Heo, J. H.; Mandal, T. N.; Seok, S. I. Chemical Management for Colorful, Efficient, and Stable Inorganic-Organic Hybrid Nanostructured Solar Cells. *Nano Lett.* **2013**, *13*, 1764−1769.
(36) Drozdowski, D.; Gągor, A.; Mączka, M. Methylhydrazinium Lead Iodide − One Dimensional Chain Phase with Excitonic Absorption and Large Energy Band Gap. *J. Mol. Struct.* **2022**, *1249*, 131660.
(37) Alberto López, C.; Consuelo Alvarez-Galván, M.; Abia, C.; Teresa Fernández-Díaz, M.; Antonio Alonso, J. Structural Phase Transitions of Hybrid Perovskites $CH_3NH_3PbX_3$ (X = Br, Cl) from Synchrotron and Neutron Diffraction Data. In *Perovskite and Piezoelectric Materials*; Pola, S.; Panwar, N.; Coondoo, I., Eds.; IntechOpen, 2021.
(38) Vegard, L. Die Konstitution Der Mischkristalle Und Die Raumfüllung Der Atome. *Z. Phys.* **1921**, *5*, 17−26.
(39) Vegard, L.; Dale, H. VIII. Untersuchungen Über Mischkristalle Und Legierungen. *Z. Krist. - Cryst. Mater.* **1928**, *67*, 239.
(40) Shannon, R. D. Revised Effective Ionic Radii and Systematic Studies of Interatomic Distances in Halides and Chalcogenides. *Acta Crystallogr., A* **1976**, *32*, 751−767.
(41) Fleet, M. E. Distortion Parameters for Coordination Polyhedra. *Mineral. Mag.* **1976**, *40*, 531−533.
(42) Spek, A. L. Single-Crystal Structure Validation with the Program PLATON. *J. Appl. Crystallogr.* **2003**, *36*, 7−13.
(43) Molak, A.; Paluch, M.; Pawlus, S.; Klimontko, J.; Ujma, Z.; Gruszka, I. Electric Modulus Approach to the Analysis of Electric Relaxation in Highly Conducting $(Na_{0.75}Bi_{0.25})(Mn_{0.25}Nb_{0.75})O_3$ Ceramics. *J. Phys. D: Appl. Phys.* **2005**, *38*, 1450−1460.
(44) Głowienka, D.; Miruszewski, T.; Szmytkowski, J. The Domination of Ionic Conductivity in Tetragonal Phase of the Organometal Halide Perovskite $CH_3NH_3PbI_{3-X}Cl_x$. *Solid State Sci.* **2018**, *82*, 19−23.
(45) Maeda, M.; Hattori, M.; Hotta, A.; Suzuki, I. Dielectric Studies on $CH_3NH_3PbX_3$ (X = Cl and Br) Single Cystals. *J. Phys. Soc. Jpn.* **1997**, *66*, 1508−1511.
(46) Yuan, Y.; Xu, R.; Xu, H. T.; Hong, F.; Xu, F.; Wang, L. J. Nature of the Band Gap of Halide Perovskites ABX_3 (A = CH_3NH_3, Cs; B = Sn, Pb; X = Cl, Br, I): First-Principles Calculations. *Chin. Phys. B* **2015**, *24*, 116302.
(47) Mączka, M.; Ptak, M.; Gągor, A.; Stefańska, D.; Sieradzki, A. Layered Lead Iodide of $[Methylhydrazinium]_2PbI_4$ with a Reduced Band Gap: Thermochromic Luminescence and Switchable Dielectric Properties Triggered by Structural Phase Transitions. *Chem. Mater.* **2019**, *31*, 8563−8575.
(48) Krishnamurthy, S.; Kour, P.; Katre, A.; Gosavi, S.; Chakraborty, S.; Ogale, S. Cystamine-Configured Lead Halide Based 2D Hybrid Molecular Crystals: Synthesis and Photoluminescence Systematics. *APL Mater.* **2018**, *6*, 114204.
(49) Yu, J.; Kong, J.; Hao, W.; Guo, X.; He, H.; Leow, W. R.; Liu, Z.; Cai, P.; Qian, G.; Li, S.; et al. Broadband Extrinsic Self-Trapped Exciton Emission in Sn-Doped 2D Lead-Halide Perovskites. *Adv. Mater.* **2019**, *31*, 1806385.
(50) Dai, J.; Zheng, H.; Zhu, C.; Lu, J.; Xu, C. Comparative Investigation on Temperature-Dependent Photoluminescence of $CH_3NH_3PbBr_3$ and $CH(NH_2)_2PbBr_3$ Microstructures. *J. Mater. Chem. C* **2016**, *4*, 4408−4413.
(51) Chen, C.; Hu, X.; Lu, W.; Chang, S.; Shi, L.; Li, L.; Zhong, H.; Han, J. B. Elucidating the Phase Transitions and Temperature-Dependent Photoluminescence of $MAPbBr_3$ Single Crystal. *J. Phys. D: Appl. Phys.* **2018**, *51*, No. 045105.
(52) Kurtz, S. K.; Perry, T. T. A Powder Technique for the Evaluation of Nonlinear Optical Materials. *J. Appl. Phys.* **1968**, *39*, 3798−3813.

https://doi.org/10.1021/acs.jpcc.1c07911
J. Phys. Chem. C 2022, 126, 1600−1610